Rice Phenology Monitoring by means of SAR Polarimetry at X-Band

Juan M. Lopez-Sanchez, *Senior Member, IEEE*, Shane R. Cloude, *Fellow, IEEE*, and J. David Ballester-Berman

Abstract—**The feasibility of retrieving the phenological stage of rice fields at a particular date by employing coherent copolar dual-pol X-band radar images acquired by the TerraSAR-X sensor has been investigated in this paper. A set of polarimetric observables that can be derived from this data type has been studied by using a time series of images gathered during a whole cultivation period of rice. Among the analyzed parameters, besides backscattering coefficients and ratios, we have observed clear signatures in the correlation (in magnitude and phase) between channels in both the linear and the Pauli bases, as well as in parameters provided by target decomposition techniques, like entropy and alpha from the eigenvector decomposition. A new model-based decomposition providing estimates of a random volume component plus a polarized contribution has been proposed and employed for interpreting the radar response of rice. By exploiting the signatures of these observables in terms of the phenology of rice, a simple approach to estimate the phenological stage from a single pass has been devised. This approach has been tested with the available data acquired over a site in Spain, where rice is cultivated ensuring ground is flooded for the whole cultivation cycle and sowing is carried out by randomly spreading the seeds on the flooded ground. Results are in good agreement with the available ground measurements, despite some limitations exist due to the reduced swath coverage of the dual-pol HHVV mode and the high noise floor of the TerraSAR-X system.**

Keywords—**Synthetic aperture radar, agriculture, polarimetry, rice, phenology**

I. Introduction

This work is centered on investigating the potential of polarimetric synthetic aperture radar (SAR) imagery acquired by satellite at X-band for identifying different phenological stages of rice fields. This approach exploits the known sensitivity of polarimetry to the structure or morphology of the observed scene in order to differentiate the physical changes and conditions followed by rice crops during its growth cycle. Since the launch of the German TerraSAR-X sensor in 2007, the availability of high resolution SAR images acquired at high microwave frequencies (X-band) and with a short revisit time (11 days) provides an excellent framework for agriculture monitoring applications. The final objective of this study consists in the development of an algorithm for estimating the phenological stage of rice fields at a particular date by using a single acquisition.

Rice has been the subject of many remote sensing initiatives due to its evident importance as basic food and economic activity in many countries, especially in South-East Asia, and its influence on global environment due to the methane emissions associated with its cultivation. Among them, successful results have been obtained with radar satellites operating at C-band (e.g. ERS, Envisat-ASAR and Radarsat-1), demonstrating that the phenological evolution of rice could be followed by time series of C-band backscatter at HH and VV channels [1], [2], [3], [4]. The C-band HH/VV ratio has been also used to discriminate cultivated fields from non-rice fields, showing a variation up to 4–7 dB from the beginning of the season to the plant maturity phase. Regarding the use of X-band, there exist also some examples of studies over rice fields conducted with an airborne experimental sensor [5] and a ground-based scatterometer [6].

To date, the long revisit time (24 or 35 days, i.e. 2 to 4 images per cultivation cycle) provided by most satellite sensors complicates the task of building an application for precise monitoring of rice phenology, especially when particular stages have to be timely identified. In order to reduce the temporal gap between acquisitions, different spaceborne SAR sensors can be combined (e.g. Envisat-ASAR and Radarsat-2) and/or different acquisition modes of the same sensors can be exploited jointly (e.g. different beams and ascending/descending orbits), despite the increased complexity in the analysis due to the influence of different system parameters and/or acquisition geometries upon the observations. Note also that in the next future the ESA Sentinel-1 satellites will provide a 6-day revisit time, hence contributing to such purposes. A second aspect not fulfilled by some sensors is spatial resolution, which may be too coarse (e.g. Envisat-ASAR after multi-looking) for specific applications. For instance, in some cases in-field heterogeneities need to be detected (e.g. cultivation problems affecting small spots with sizes of 10–20 m).

Besides high spatial resolution and short revisit time, TerraSAR-X provides a key enhancement in the polarimetric information content with respect to previous dual-pol systems, such as Envisat-ASAR, because it acquires the two copolar channels (HH and VV) in a coherent way. Note that many satellite sensors do not provide coherent polarimetric information, and Sentinel-1 will offer coherent but only with one copolar and one crosspolar channel, not both copolar. As a result, with TerraSAR-X the phase between both channels is an additional observable which can be exploited for crop classification or crop condition discrimination [8], [9]. More importantly, this phase information enables the change of the polarization bases for representing the data, which is useful to interpret the information provided by the radar data and, specifically, to compute parameters (observables) with clear physical meaning [10]. In particular, the well-known eigenvector decomposition and a model-based decomposition of the 2x2 coherency matrix will be used in this work to facilitate the interpretation of the radar observations as a function of rice phenology.

Juan M. Lopez-Sanchez and J. David Ballester-Berman are with the Dept. of Physics, Systems Engineering and Signal Theory (DFISTS), University of Alicante, P.O.Box 99, E-03080 Alicante, Spain (e-mail: juanma-lopez@ieee.org, davidb@ua.es). Shane R. Cloude is with AEL Consultants, 26 Westfield Avenue, Cupar, Fife, KY15 5AA, Scotland, UK (e-mail: aelc@mac.com).
This work was supported by the Spanish Ministry of Science and Innovation (MICINN) and EU FEDER, under Projects TEC2008-06764-C02-02 and TEC2011-28201-C02-02, and Grant PR2009-0364 of the National Program of Human Resources Movability, by the University of Alicante under Project GRE08J01, and by Generalitat Valenciana under Projects GV/2009/079 and ACOMP/2010/082.

Recently, we have shown some initial results about the potential of TerraSAR-X dual-pol imagery for rice monitoring [7]. The current work is intended to confirm that potential by developing a real monitoring application and by extending the previous analysis to other important observables provided by this imagery. A time series of HHVV dual-pol images of TerraSAR-X acquired in 2009 over a test site in Spain, and a complementary ground campaign are employed in this work.

In principle, the main drawback of using dual-pol TerraSAR-X images for this application is their narrow swath (around 15 km on the ground), which is too small for devising a monitoring scheme on large scale rice plantations. A second limitation that will be found is the noise level of the system (NESZ around -19 dB), which may result very close or even higher than the backscattering from rice fields, especially at the early stages of the cultivation cycle.

Regarding the final application, it is necessary to define the scope of this study. The original motivation of this work comes from farming practices in rice fields over temperate regions, like Spain. In these scenarios, timely information about crop condition and development status of parcels (and also different areas within a parcel) is helpful for planning and/or triggering farming activities. For instance, detecting the moment with full emergence of the plants is commonly employed by farmers to go to the fields and count the number of plants or the so-called *effective germination*. If the value is lower than expected, they still have an opportunity to sow again in order to increase the plantation density and, consequently, the final yield. As a second example, knowing that crops have arrived at the end of the vegetative phase is also important for stopping the application of fertilizers, since they are not longer useful and, when applied in excess, they can also lead to pest problems by increasing the birth rate, longevity and overall fitness of certain agricultural pests. A third clear example, possible when high spatial resolution is provided in the phenological information, consists in identifying different growth rates within the same fields. This information is also of interest for farmers in order to optimize resources or, in some cases, to detect phenological delays caused by cultivation problems, such as water salinity and plagues. Finally, phenology is useful as an input in crop growth and yield prediction models. In summary, the final objective is the estimation of the current phenological stage of rice fields to help these farming practices. In this context, it is important to note that the location and areas of the fields to be monitored are provided by the farmers, so they are assumed to contain rice plants and no other species. Therefore, rice mapping is not regarded as an application of this study, and the potential presence of mixed species in some fields would be treated as cultivation problems at the corresponding rice fields.

Due to the diversity of rice cultivation practices, it is also necessary to define the focus of the study on the region where data are available (both ground measurements and SAR images), i.e. Spain and similar regions. As will be commented in next section, there are many particularities due to varieties of rice and to farming practices which need to be taken into account when establishing the conclusions of this study and its potential translation to other areas. Evidently, due to the lack of data, a worldwide global application of the conclusions of this study is out of our scope for the moment. Instead, comments regarding the hypotheses to be fulfilled for establishing the applicability of this work will be included in the text.

The text is organized as follows. Section II introduces briefly the terminology and the numerical scale employed for describing the phenology of rice. The main stages in the growth cycle are also presented in this section. Then, the test site, ground data and the radar images available in this research are detailed in Section III. Section IV presents the observations provided by a wide set of polarimetric observables, together with their analysis and a discussion about their physical interpretation. From that discussion, Section V proposes and tests a simple approach for estimating the current rice phenological stage from the radar data. Finally, the main conclusions and future activities in this field are summarized in Section VI.

II. Phenology of rice

Three main stages are usually defined for the rice growth cycle: *vegetative*, *reproductive* and *maturation or ripening*, each of them with particular features and aspects of the plant development as a function of time. This temporal evolution can be better described by identifying a larger number of main stages which are subsequently subdivided into secondary stages in order to provide a continuous numerical scale of the plant phenology. A widely employed scale of such type is the general BBCH scale (from *Biologische Bundesanstalt, Bundessortenamt und CHemische Industrie*) for cereals [11], [12], which provides also a particular representation for rice. The principal stages and the corresponding numerical ranges are introduced in Table I. The first half of the cycle, from stage 0 to 49, corresponds to the mentioned vegetative phase, whereas stages 50 to 69 and 70 to 99 constitute the reproductive and maturation phases, respectively.

The description in terms of the BBCH scale is based on the actual characteristics of an individual plant. When the scale is used for the definition of the development stage of a plant stand or parcel, the description should apply to at least 50 % of the plants inside the parcel. Therefore, a specific field or parcel will be considered to reach a particular BBCH stage when more than half of its plants reach that stage. This criterion has to be taken into account when analyzing the ground measurements and when studying the radar images, since we will show that plant development is quite heterogeneous inside some parcels at some stages of the campaign.

The vegetative phase comprises a wide range of plant conditions, starting from germination and finishing with fully developed plants. In a few words, it is characterized by an increase of the plants height (up to 70–90 cm), an increase in the number of tillers, and the development of leaves in the top part (flag leaves). During the germination (BBCH 00-09), the development is centered on the seed and the radicle. Then, at BBCH 10 the first leaf is clearly visible and additional leaves are unfolded up to stage BBCH 19. The tillering phase, from BBCH 21 to 29, is defined by the progressive detection of the first (at BBCH 21) and additional tillers (up to a maximum number at BBCH 29). Afterward, there is an extension of all elements (BBCH 30-39), and at booting (BBCH 40-49) the upper part of the stems thickens and the flag leave opens. During all these stages the

TABLE I
BBCH SCALE DESCRIPTION OF RICE PHENOLOGY

Principal stage	BBCH	Name
0	00-09	Germination
1	10-19	Leaf development
2	20-29	Tillering
3	30-39	Stem elongation
4	40-49	Booting
5	50-59	Heading, inflorescence emergence
6	60-69	Flowering, anthesis
7	70-79	Development of fruit
8	80-89	Ripening
9	90-99	Senescence

TABLE III
INFORMATION ABOUT THE TERRASAR-X SLC IMAGES

Mode	Stripmap
Beam	StripNear007
Avg. Incidence angle	30 degrees
Polarization channels	HH and VV
Orbits	Ascending
Time of acquisition	6:15 pm
Center frequency	9.65 GHz
Slant-range pixel spacing	0.909 m
Slant-range resolution	1.177 m
Slant-range oversampling	0.77
Azimuth pixel spacing	2.587 m
Azimuth resolution	6.6 m
Azimuth oversampling	0.392

plant structure remains erectophile, with almost vertical stems and with leaves presenting small inclination angles (up to 20 degrees approximately), although this depends on rice varieties.

The next main stage (reproductive) starts with the emergence of the panicle, being the heading phase (BBCH 50-59) defined by the progression of this emergence until its completion. Then, during the BBCH 60-69 the anthers appear and fully develop. The plant height does not increase significantly and eventually remains constant at 95–100 cm. These phases are characterized by a general increase in the number of elements in the top part of the plant, and leaves increase their inclination angles, hence loosing the erectophile condition and tending to be more random. In addition, the stems become drier and tend to present a cane structure.

Finally, the maturation or ripening stage constitutes also a period with many changes in the plants. Grains appear and become milky (BBCH 70-79) and then dough (BBCH 80-89). The last stages until harvest depend mostly on the moment chosen for harvest (the water content of the grains changes up and down until it is about 18-22 percent at optimum harvest time), but in general all plants become drier and their full structure is mostly random, with a decrease in the number of leaves.

After this general description of the phenology of rice, all details about the specific test site, the ground measurements campaign and the analyzed images are presented in next section.

III. TEST SITE, GROUND MEASUREMENT CAMPAIGN AND SAR DATA

The test site consists of an area of 30 km x 30 km in the mouth of the Guadalquivir river, Seville, SW of Spain, where rice is cultivated annually from May to October, approximately. General rice species in this area is *Oryza sativa L.*. The specific variety cultivated in the monitored fields corresponds to a long grain type named *puntal*, quite common in Spain and other similar temperate regions.

Cultivation practices are very diverse all over the world, so the farming procedure in this area has to be defined. For instance, cultivation may be initiated by transplanting, wet sowing or dry sowing. Moreover, fields can be drained during the cultivation cycle or not. Finally, growth cycle can be very short (e.g. 80 days) or much longer (up to 150 days) depending on the practices and the region. In this test site sowing is carried out by spreading seeds randomly from an airplane over the fields, which are already flooded at that time. Then, farming practices in this area ensure the presence of a water layer on the ground during the whole cultivation period, hence the ground is always flooded. Finally, the cultivation campaign lasts about 135–150 days. These aspects are very important in order to analyze the radar response from the scene, as will be commented in next sections.

During the 2008 and 2009 campaigns, the local association of rice farmers (*Federacion de Arroceros de Sevilla*) collected detailed ground measurements on a weekly basis. For this research project, centered in the 2009 campaign, 6 specific parcels, spread over the whole site, were selected for intensive sampling.

The weekly measurements include phenological stage and total vegetation height. In addition, the following information is known for each parcel (see Table II): total area (ha), sowing date, surface density of plants (plants/m^2) and panicles (panicles/m^2), harvest date, and final yield (kg/ha). Specific aspects for some of them have been registered also, such as irrigation conditions, water salinity and presence of plagues.

Regarding the parameters displayed in Table II, note that neither sowing nor harvest are simultaneous in all parcels of the site, being around 3 weeks time span between the first and the last of the monitored parcels in both activities. The large variability observed in plant density (e.g. from 315 to 850 plants/m^2) is due to the local conditions at the time of sowing. Despite the procedure is nominally common to all fields in the test site, the following specific aspects at the time of sowing may affect importantly the final plant density: wind and temperature, quality of irrigation water, eventual drainages, plagues incidence, presence of another herbs and seaweed, etc.

In order to maximize the data acquisition of TerraSAR-X images over the test site, a set of three parallel time series were set up originally. Each time series, with an 11-days revisit period, corresponds to HHVV dual-pol stripmap images obtained with a different incidence angle, namely 22, 30 and 40 degrees. Due to space constraints, the analysis presented in this paper is limited to the case of 30 degrees, leaving the angular dependence of the results for a future publication. The main information of these images is presented in Table III. Due to the narrow swath of these dual-pol images (15 km) parcel D falls outside their coverage, so the analysis presented here is restricted to the remaining five parcels.

The final schedule of the 15 images acquired at 30 degrees

TABLE II
DESCRIPTION OF THE MONITORED PARCELS

Label	Surface (ha)	Sowing date (DoY)	Plants/m^2	Panicles/m^2	Harvest date (DoY)	Yield (kg/ha)
A	13.14	17-may (137)	315	530	07-oct (280)	8.949
B	12.47	15-may (135)	350	600	29-sep (272)	8.729
C	40.5	7-may (127)	850	1300	25-sep (268)	10.400
D	7.57	6-may (126)	345	608	25-sep (268)	9.000
E	4.34	24-may (144)	400	512	08-oct (281)	10.060
F	17.26	15-may (135)	450	580	14-oct (287)	9.000

is illustrated in Fig. 1 together with the phenological evolution of the monitored parcels. The first image was acquired on May 17 (DoY 137) and the last one on October 18 (DoY 291). The BBCH evolution of these parcels shows a clear common trend, but there are also important differences between parcels which need to be taken into account when analyzing the radar data, since some of them develop faster than others at some stages.

Some comments about the BBCH evolution and the observation scheme are in order (Fig. 1). On the one hand, there are dates (especially around DoY 230–240) with differences about 30 BBCH values between parcels. On the other hand, there are BBCH intervals (e.g. 19 to 23) where some parcels last about 4 weeks. A simple linear interpolator will be employed for deriving the BBCH at the dates of the radar acquisitions, since the acquisition dates are not coincident with the ground campaign dates. This assumption constitutes an uncertainty source because the temporal evolution of BBCH may not be linear in many cases. This can be especially relevant in some transitions between BBCH stages, since, as commented in Section II, a BBCH value is assigned to a parcel when more than the 50% of the plants belongs to that stage, despite there are other plants more advanced or delayed.

Finally, there is also climate information provided by the Spanish Government under the *Sistema de Informacion Agroclimatica para el Regadio (SIAR)*, including daily files of temperature, precipitation, humidity and wind. In this region, a rainy season is common at the beginning of autumn every year. During 2009, the first important precipitation of the season took place on September 13 (DoY 256), and there were frequent rains for a month. Consequently, all images acquired from that date were strongly affected by either the presence of rain or the increased water content in the plant volume due to previous rain. As a result, the radar response from the rice fields was very distorted, showing a large increase in the backscattering levels and changes in other polarimetric observables with respect to days without rain (also in the rest of the scene, including bare fields). Therefore, all images acquired after that date have not been considered in the analysis performed in this work. In parallel, the acquisition of ground measurements finished on September 17 (DoY 260), when almost all parcels had reached BBCH 90, and harvest started to be planned.

Once all the available data have been presented, next section describes the analysis carried out with them, with a main focus on the sensitivity of polarimetric observables upon the phenological features of the monitored rice fields.

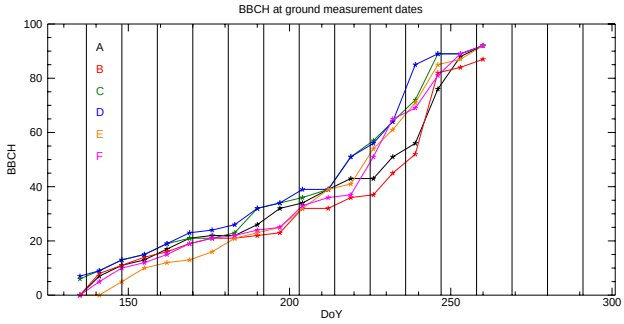

Fig. 1. Evolution of the phenology at the six monitored parcels as acquired during the ground campaign, plotted as a function of day of year (DoY). Vertical lines denote the dates of acquisition of the TerraSAR-X images

IV. ANALYSIS OF THE POLARIMETRIC RESPONSE AT 30 DEGREES

This analysis is focused on the evolution of the observables for the monitored parcels over the whole growth cycle. For each parcel we defined its corresponding region of interest (ROI) in the images and the averaging of the coherency/covariance matrix was performed with all the values inside the ROI. Therefore, we estimated one averaged observation for each parcel. Then, all the polarimetric observables to be analyzed have been computed for all the images and plotted as a function of the phenological stage (BBCH value). It is necessary to note that since the original images are highly oversampled, especially in azimuth, the number of effective looks is much lower that the number of original pixels. At 30 degrees each original pixel corresponds to 0.3 looks. However, these observations generated by averaging over a whole parcel are well estimated, since parcels occupy from 8000 to 80000 pixels approximately (see exact areas in Table II), so the number of looks is always extremely large.

Figure 2 presents the plots of the observables analyzed in the following, computed for all the monitored parcels. We present twelve key parameters from our analysis, divided into six main categories as follows.

A. Backscattering coefficients and ratio

The normalized backscattering coefficients are the most basic products provided by any radar. In our case, the copolar HH and VV channels are available, usually denoted as σ^0_{hh} and σ^0_{vv} (Fig. 2a).

It is important to comment that the TerraSAR-X images can be calibrated in two different ways. The conventional calibration [13] allows the translation of DN (for detected products)

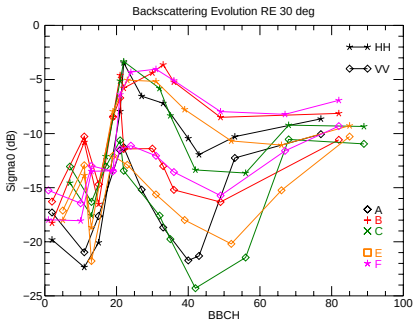

(a) Backscattering coeffs.

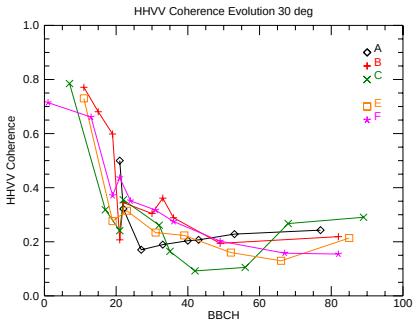

(b) Coherence between HH and VV

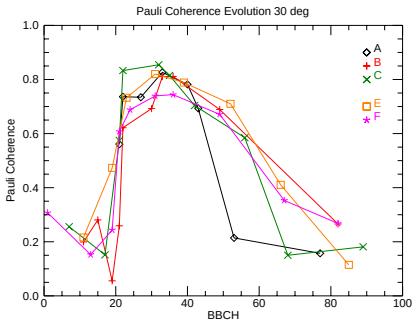

(c) Coherence between Pauli 1st and 2nd

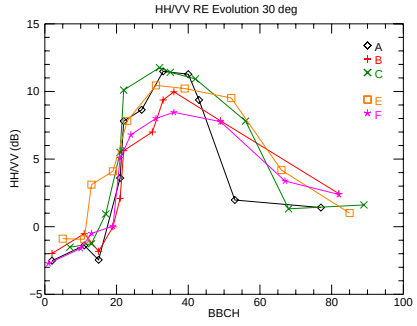

(d) HH/VV ratio

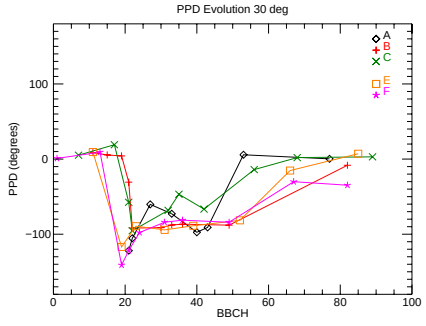

(e) Copolar phase difference

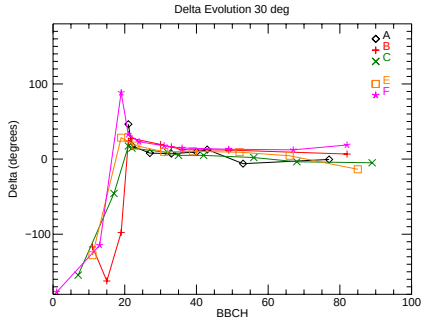

(f) Phase diff. between Pauli 1st and 2nd

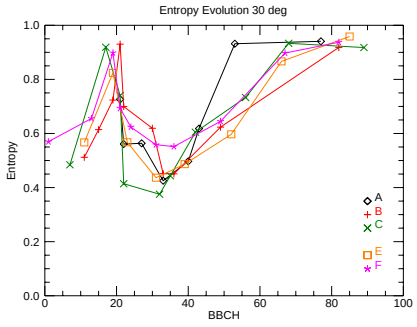

(g) Entropy

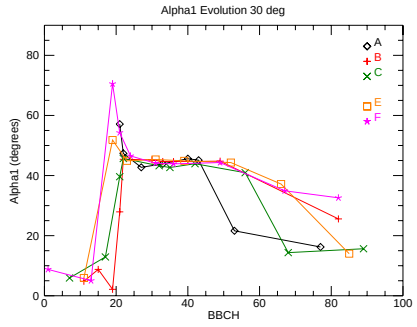

(h) Dominant α

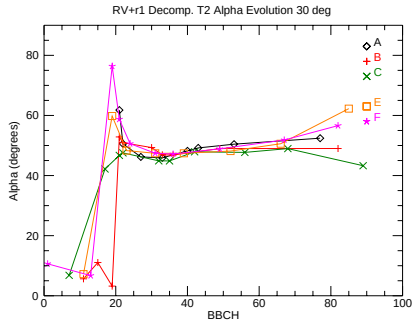

(i) α_P (polarized term angle)

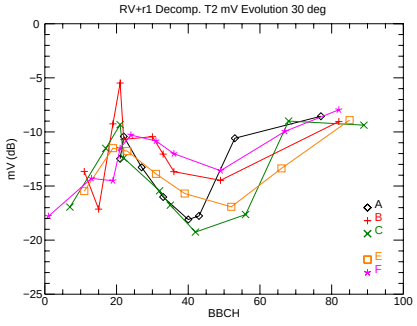

(j) Volume term m_V

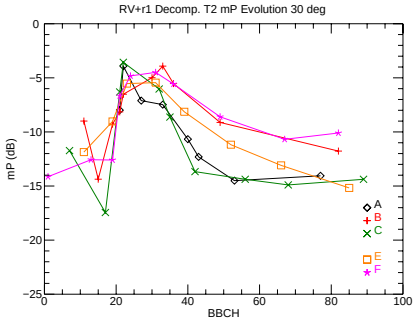

(k) Polarized term m_P

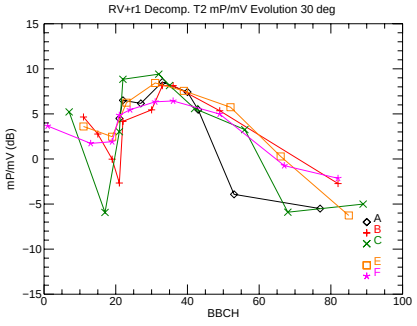

(l) m_P/m_V ratio

Fig. 2. Polarimetric observables at 30 degrees for the monitored parcels as a function of BBCH

or complex values (for single-look complex products, as in this case) to β^0 and σ^0, and can be performed on a pixel-by-pixel basis. The second possible calibration, named radiometric enhanced (RE) [14], consists in computing the backscatter power using an spatial window (multi-looking) and then subtracting a noise estimation annotated in the product headers. The RE calibration is necessary when working with low backscattering values, specially those close to or lower than the noise level. The drawback of the RE calibration is that it can be only performed on multi-looked power images, so the phase information is not available anymore in the calibrated results and spatial resolution is slightly degraded. In our case, the VV coefficient can be close to or lower than the NESZ of the system (around -19 dB for these images) at several phenological stages, and also the HH coefficient at the early stages, so the RE calibrated data will be employed when analyzing the copolar backscattering coefficients and their ratio. For all other polarimetric observables the conventional calibration will be used, but they will not be considered (hence not displayed in Fig. 2) when their corresponding backscattering coefficients are below -16 dB, since noise would be contaminating their estimation.

At the beginning of the campaign (until the plants emergence before BBCH 20 approximately) the absolute backscattering levels are low (below -10 dB), as expected from a flooded ground surface, but they change importantly from date to date and from parcel to parcel. The increased backscattering at some cases is due to the presence of wind and the resulting induced roughness. Note that the monitored parcels are quite separated over the site and they exhibit different degrees of protection against wind. In addition, the horizontal axis in these plots is BBCH, not date, so for the same phenological stage parcels may be affected or not by wind, depending on the conditions on the date they reach that BBCH value.

At BBCH 20 approximately, when plants clearly emerge above the water level, the responses of both HH and VV increase significantly, and they reach their maxima before BBCH 30. The maximum backscattering at horizontal polarization is -4 dB, whereas it is only -11 dB at vertical polarization. It will be shown to be a dihedral response in Section IV-E, produced by the interaction between the flooded ground and the stems, and before extinction becomes important (plants are not tall and dense enough at this stage).

From BBCH 30 the five parcels show a clear and almost linear decrease in both copolar responses, as a result of the increasing vegetation height and the effect of extinction, but they exhibit different slopes or decreasing rates. The fastest ones reach the lowest levels at BBCH 40-45 for both channels, whereas the slowest reach the minimum levels at BBCH 50. The minimum levels differ from parcel to parcel, up to 5 dB for HH and 8 dB for VV. From this stage, when plants start to become more random than before, all parcels increase monotonically their backscattering levels until the end of the growth cycle, again with different change rates, and providing values between -7 and -11 dB at BBCH 80, HH being slightly higher (1-2 dB) than VV. Differences between parcels can not be explained only by the different plantation densities (see values in Table II, in plants/m^2 or panicles/m^2), and other physical features at local level are influencing the observed radar backscatter.

The evolution described for both channels can be jointly exploited by observing their ratio, shown in Fig. 2d. At the beginning of the season, without the emerged plants, the Bragg scattering from the rough surface of the flooded ground predicts VV larger than HH, and accordingly the ratio is between -3 and -1 dB. Then, the presence of the double-bounce generates a sudden increase in HH/VV, reaching 5 dB at BBCH 21-22 and maximum values from 8 to 12 dB at BBCH 30-35. After a short plateau, the HH/VV ratio decreases monotonically towards the end of the cycle, giving values of 1 to 2 dB at BBCH 80. This gentle decrease is produced by the different trends and change rates in the HH and VV channels, as commented before.

The HH/VV intensity ratio constitutes an excellent indicator of the presence of rice. This parameter was used in [4] at C-band for discriminating cultivated fields from non-rice fields, based on a dynamic range of up to 4–7 dB. At X-band the dynamic range is larger (8–12 dB), hence providing an even better estimation accuracy.

B. Coherence between HH and VV

The correlation between HH and VV, $|\rho_{hhvv}|$, defined between 0 and 1, exhibits two regions of values (Fig. 2b). At the beginning of the campaign the dominating surface scattering is characterized by a high correlation between the two copolar channels, with values always above 0.6. Then, as soon as the plants emerge the coherence between the two copolar channels drops and remains below 0.4 for the rest of the rice growth cycle. The low magnitudes of ρ_{hhvv} are caused initially by the extreme differential extinction, which attenuates severely the VV channel with respect to the HH. Then, an increase of random volume scattering at the later stages drives this parameter, since only a small correlation between polarimetric channels is expected from that scattering type (theoretically $\rho_{hhvv} \approx 1/3$).

C. Phase difference between HH and VV

The phase difference between the copolar channels, $\Delta\phi$, also named as *polarization phase difference, PPD*, or *copolar phase difference, CPD*, is known to be useful for crop classification or crop condition discrimination [8], [9]. In our case (see Fig. 2e), it is consistently around zero at the beginning of the season, again as a result of the dominant surface scattering. Then, a very clear jump is observed around BBCH 19–21, corresponding to the presence of enough double-bounce scattering to dominate over the surface scattering. This is a consequence of the emergence of the plants above the water level. The minimum phase value reached at this point ranges from -90 to -140 degrees, showing important differences from parcel to parcel and from date to date. From that stage, despite some fluctuations for two of the monitored parcels, it remains at around -90 until BBCH 50. Finally, the more heterogeneous backscattering present from that stage, due to the increase of volume scattering, produces a trend in the phase difference, which approaches a zero value, but with a large variability at the end of the season. The variability of this parameter at the end of the season is expected as a result of the random volume morphology of the scene, which produces a wide distribution of phase difference values with zero mean.

The mentioned jump at plants emergence was already noticed in [7]. However, the measured values of the phase difference before plants emergence were around 30 degrees, instead of the null value shown here. The cause of this discrepancy is that TerraSAR-X images processed before April 2010 were not properly calibrated since the phase induced at each channel by the antenna pattern corresponding to each beam (where the beam defines the range of incidence angles) was not compensated [15]. Fortunately, the phase distortion and its compensation are stable in time for each beam, so the phase compensation carried out (and annotated as auxiliary files) in the images processed after April 2010 has been successfully applied to the archived images. After the mentioned compensation, the phase difference is always around zero before the emergence time for all incidence angles, as expected from theory. Therefore, the jump at emergence time is better defined, and the values after that moment can be analyzed for monitoring purposes.

In order to illustrate the performance of the copolar phase difference for the detection of plants emergence, Figure 3 shows both the HH backscattering coefficient and the phase difference at the location of parcel F for three consecutive dates: DoY 148, 159 and 170. For such purpose, a rectangular portion of the images in slant-range azimuth coordinates has been extracted and the averaging for multi-look and estimation has been performed by means of an 11x11 boxcar window. This window size provides an equivalent number of looks around 36 at 30 degrees, which is slightly low, but enough to provide an insight about the values of the observables. Note that this figure is for illustration purposes only, and other filtering strategies, specifically those preserving the edges among parcels, should be employed in a final application [16].

The phenological stage for parcel F in Figure 3 was measured as BBCH 10 on DoY 148, BBCH 12 on DoY 155, BBCH 15 on DoY 162, BBCH 19 on DoY 169 and BBCH 21 on DoY 176, hence these acquisitions correspond to the time of emergence of the plants. This parcel is formed by 4 sub-parcels of rectangular shape located in the center of the image. At the first two images the HH backscattering coefficient shows some areas inside the sub-parcels with higher values as a consequence of wind induced roughness on the flooded ground, but the phase difference remains stable independently of these magnitude variations. In the third image the subparcels exhibit a higher contrast between high and low power values, since most of this parcel is now covered by plants. This is better confirmed by the phase difference, which drops very clearly to negative values over the vegetated areas.

Despite the easy interpretation of the main features and stages of this parameter in terms of the rice phenology, the actual values are not as easily predicted. This aspect was discussed in some detail in [7], and a general model for this parameter and this general type of scene with a dominant double-bounce under vegetation can be consulted in [8].

D. Pauli coherence and phase difference

The coherence between the first and the second Pauli channels, HH+VV and HH-VV, also named Pauli coherence, $|\rho_P|$, is analyzed for the first time in this work and it presents an evident signature in terms of the phenology of the rice plants (see Fig. 2c). It is very low (under 0.3) at the early stages because, as commented earlier, HH and VV are highly correlated and have a null phase difference between them. Therefore, the two Pauli channels are very different in amplitude. This situation changes dramatically from BBCH 20, when plants emerge, reaching very high coherence values (around 0.7-0.8 for all parcels). From BBCH 40 the Pauli coherence decreases progressively until the end of the season.

The physical interpretation of the Pauli coherence from BBCH 20 can be found in the previous analysis of the backscattering powers, and more precisely in the low values of the VV channel in comparison with HH (due to both the double-bounce and the differential extinction). When VV is very low the two Pauli channels are very similar to the HH channel and, consequently, are very correlated. This situation, as already commented, tends progressively to disappear towards the end of the cultivation cycle. Note also that the phase difference between the Pauli channels (named δ angle) is also around zero from BBCH 20 to the end of the season (Fig. 2f).

When comparing Figures 2c and 2d, it is clear that the evolution of the Pauli coherence in terms of the BBCH scale perfectly matches the evolution of the HH/VV intensity ratio. In fact, they could be considered as scaled versions of the same observation, since their shape is almost the same. This confirms the above comments about the influence of backscattering level differences between HH and VV on this observable.

E. Entropy and dominant alpha angle

The eigenvector decomposition of the coherency matrix provides additional information to help the interpretation of the observed radar response of rice at its different stages, as will be explained here. Due to the dual-pol acquisition, a 2x2 coherency matrix is available, and all the derived parameters are defined accordingly, such as entropy and alpha angle [17]. First results on rice fields produced by the $H2\alpha$ classification were presented in [7]. It was shown that the presence of grown rice fields (e.g. at the second half of the vegetative phase) was described by a low entropy and an average alpha angle around 45 degrees. This combination means that scattering is dominated by a single scattering type, and that this type is dipole-like. Dipole-like scattering is characterized by a linearly polarized scattered electromagnetic field, which in this case is generated by the strong differential extinction mentioned above. In this work we complete the study by applying this decomposition to all phenological stages and hence analyzing the whole evolution of entropy and α_1 (dominant scattering mechanism).

Entropy presents a distinct response with respect to the rest of the observables analyzed so far (see Fig. 2g). At the beginning of the growth cycle, entropy is low (below 0.6) since the only scattering mechanism present in the scene is the one from the rough water surface. This is confirmed by the value close to 0 of the α_1 angle, which corresponds to surface-type scattering (see Fig. 2h). When plants emerge, around BBCH 20, we suddenly measure a very high entropy (around 0.9) which is an indication of the presence of (at least) two types of scattering types inside the parcel. The first type corresponds to the mentioned surface scattering, and the second one is the new double-bounce type appearing as a consequence of the plants emergence. According

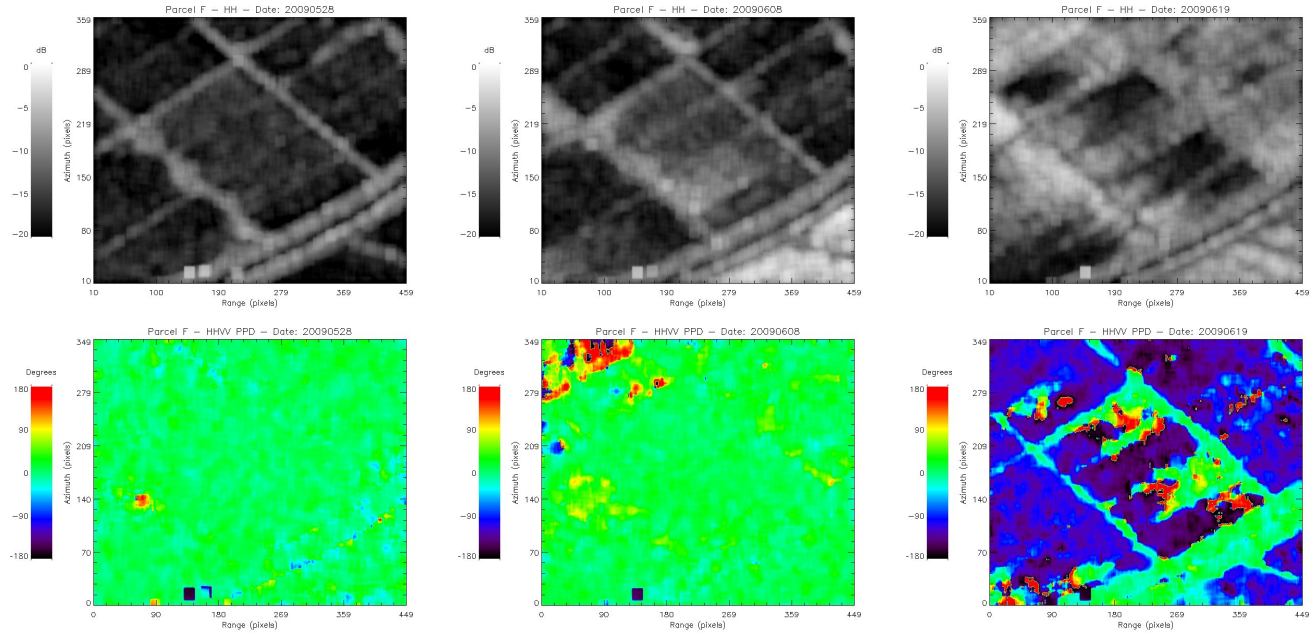

May 28 (DoY 148) June 8 (DoY 159) June 19 (DoY 170)

Fig. 3. HH Backscatering coefficient (top row) and copolar phase difference (bottom row) at parcel F, at three consecutive dates: May 28 (DoY 148), June 8 (DoY 159) and June 19 (DoY 170). A boxcar window of 11x11 pixels (ENL = 36) has been applied for speckle filtering and averaging. This parcel is formed by 4 sub-parcels of rectangular shape located in the center of the image.

to the practical measurement of entropy, this means that the two scattering mechanisms are present in the set of pixels employed when averaging the coherency matrix. In this case we are using all the pixels of the parcel for averaging, so a high entropy can be the result of observing either two mechanisms at the same positions (pixels) or different phenological stages at different positions within the parcel. This second case is a very common situation, since not all the plants develop at the same rate and hence many times some areas are more developed than others. Indeed, the definition of the BBCH value for a parcel, instead of for a plant, takes this situation into account by stating that the BBCH of the parcel is defined by the BBCH value reached by more than 50% of the plants in the parcel. Note also that the problem of getting high entropies due to scene heterogeneity is known and, in practical applications, the averaging window is restricted to ensure homogeneous areas.

In order to illustrate the behavior of entropy and α_1 around BBCH 20, Figure 4 presents three images corresponding to both parameters over parcel F and surroundings, acquired on DoY 159, 170 and 181, respectively. The phenological stage was measured as BBCH 12 on DoY 155, BBCH 15 on DoY 162, BBCH 19 on DoY 169, BBCH 21 on DoY 176, and BBCH 22 on DoY 183. In the first image, entropy is low over the whole parcel. Then it increases over most of the parcel surface in the second image. Finally, in the third image most of the parcel area exhibit low entropy, but there are places with high entropy too. Again, this heterogeneity is expected as a consequence of the different development rate of the plants within the parcel.

After the mentioned increase in entropy just before BBCH 20, it then falls to low values for the rest of the vegetative phase (say BBCH 25–50). This means that backscattering is then observed as dominated by a single mechanism. The observed scattering mechanism from BBCH 25, as provided by α_1, is dipole-like, which in this case is generated by an extreme differential extinction which makes the scattered wave to be linearly polarized. Therefore, despite the dominant scattering mechanism is the double-bounce interaction between stems/tillers and flooded ground, which is normally characterized by α close to 90 degrees, we are observing α around 45 degrees. A quantitative description of this effect of the differential extinction is provided in [10]. Differential extinction distorts the scattering mechanism generated under the vegetation volume. In this sense, the vertically oriented volume formed by rice plants during this stage acts like a polarization filter. Note also that from BBCH 19 to 25, approximately, the retrieved α_1 is above 45, even reaching 70 degrees. At these stages the differential extinction is not so severe (plants are not tall and dense enough) and the double-bounce is clearly observed before the polarization filter starts to act. This aspect can be observed in the bottom row of Figure 4. In the first image all the parcel pixels correspond to surface-type scattering. Then, as plants emerge, there appear spots with α_1 clearly above 45 degrees, corresponding to double-bounces. As plants continue to develop, as in most of the parcel at the third image, α_1 tends to 45 degrees. Note also that the less developed areas in the image on DoY 170 (around pixel 300,160 in range,azimuth), with surface scattering at that date yet, present a double-bounce scattering on DoY 181, like the rest of the parcel had reached before.

At the end of the vegetative phase, entropy starts to increase, and it maintains an almost linear trend up to the end of the growth cycle. The progressive increase of volume scattering, together with the reduction of the differential extinction and its polarization filtering effect, are the origin of this trend. The high entropy at the end of the season is produced by the random scat-

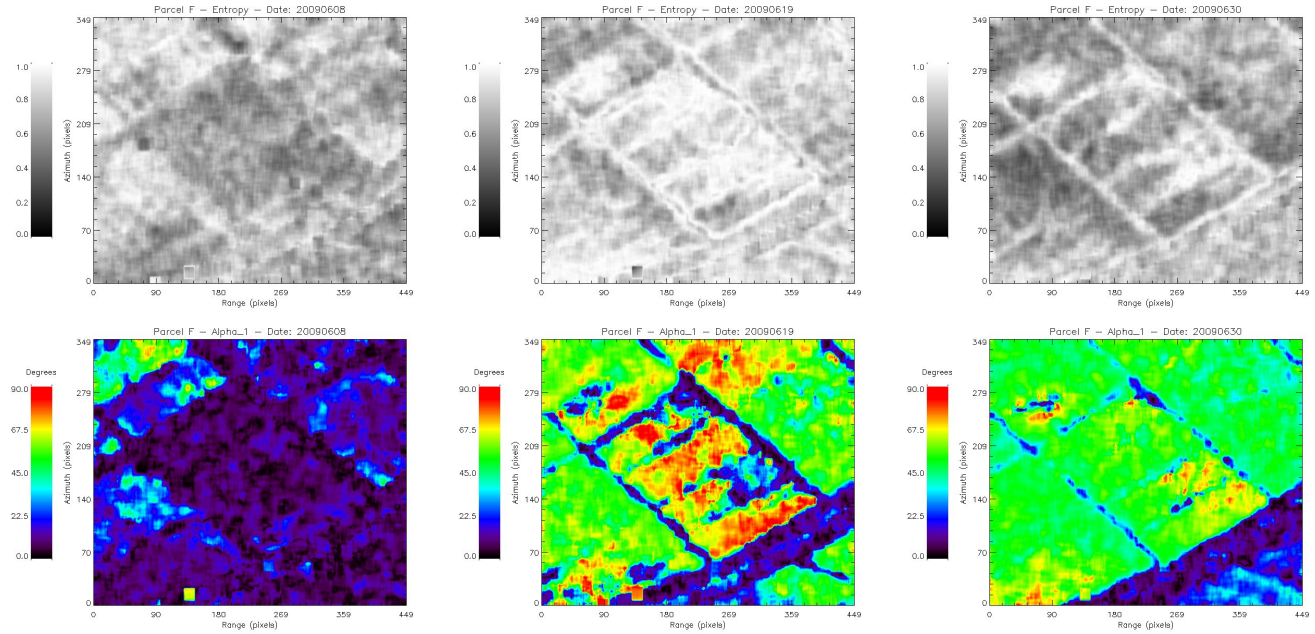

June 8 (DoY 159) June 19 (DoY 170) June 30 (DoY 181)

Fig. 4. Entropy (top row) and α_1 (bottom row) at parcel F, measured at 30 degrees incidence at three consecutive dates: June 8, 19 and 30 (DoY 159, 170 and 181). A boxcar window of 11x11 pixels (ENL = 36) has been applied for speckle filtering and averaging. This parcel is formed by 4 sub-parcels of rectangular shape located in the center of the image.

tering generated by the plants volume, so in this case it should not be interpreted as the result of two scattering mechanisms present in the scene, but due to the presence of extreme depolarization. Therefore, despite we can measure high entropies (around 0.9) both at the plants emergence stage (BBCH 18–21) and at the end of the season (BBCH 70+), their physical origin is completely different. This ambiguity in the interpretation of dual-pol measurements is well-known in polarimetry and is related to the concept usually referred as *the wave dichotomy* [10]. For our purposes, this dichotomy may constitute a source of ambiguity at the moment of exploiting entropy for estimating by itself the BBCH value of a rice field, since we cannot distinguish between the two situations despite they are very different in origin. Anyway, other observables (as will be shown in Section V) can complement this information and solve the ambiguity for retrieving the right phenological stage. Note that this ambiguity could be solved with a fully polarimetric system, since additional parameters, like anisotropy, may allow us to distinguish between both scenarios. It is also necessary to remember that high entropies are an indication of low information content in the polarimetric measurements.

Finally, note that from BBCH 50 the dominant scattering mechanism, as provided by α_1, is not dipole-like or 45 degrees anymore. The retrieved values, all below 45 degrees, correspond better to surface-type, but still affected by extinction. This region between pure surface (0 degrees) and pure dipole (45 degrees) is usually named as anisotropic surface, because HH and VV tend to be in phase but one is still larger than the other.

F. Observations from a model-based decomposition

From the previous description of the radar response of the rice fields one can conclude that the following scattering mechanisms will be present in the scene:

- Direct surface scattering from the flooded ground, due to wind induced roughness, mostly in the early stages (BBCH 0–20).
- Double-bounce interaction between stems/tillers and the flooded ground, starting at plant emergence (BBCH 20+). This mechanism will be severely affected by differential extinction and differential phase shifts at the vegetation volume, especially at the vegetative stage (BBCH 20–50).
- Volume scattering from the leaves and other plant elements. This scattering source is expected to change its features as a function of the randomness of the volume, starting as an oriented volume (OV) when plants are mostly erectophile and tending to a random volume (RV) as they develop and reach later phenological phases. The amount of volume scattering should increase progressively as plants grow and more elements appear in their upper part (especially from BBCH 45–50).

Therefore, the objective consists in estimating the amount and characteristics of each one of these mechanisms, as a function of phenology, by decomposing the measured coherency or covariance matrices[1]. This task is well known in POLSAR applications for vegetated scenes, especially in forestry, and there exist several decomposition approaches for such purposes, globally named as model-based decompositions [18], [10]. However, these approaches are generally designed for fully polarimetric data, not for dual-pol data as in this study. Therefore, an adapted decomposition is proposed in this paper providing two components: a random-volume term, with amount m_V, plus a rank-1 or polarized scattering term, with amount m_P and described by its scattering-type angle (α_P) and an auxiliary phase (ϕ_P). The derivation of this decomposition is included in the Appendix.

[1]The coherency matrix notation is used here for convenience, but similar approaches can be designed for the covariance notation

The amount of the volume (m_V) and the polarized (m_P) contributions, and their ratio, are plotted in dB in the last row of Figure 2. Moreover, the alpha angle retrieved for the polarized component (α_P) is shown in Figure 2i.

After a first BBCH interval where the model assumptions do not fit the scene components (e.g. there are two polarized components as previously shown in the entropy analysis), the signature of the model parameters from BBCH 20 to the end of the season provides some extra information as well as confirmation of previous comments when interpreting the evolution of the radar response from rice. A straightforward way to interpret these observations is through the m_P/m_V ratio (Fig. 2l) and the α_P angle (Fig. 2i). The behavior of the m_P/m_V ratio from BBCH 20 resembles quite well the evolution of the HH/VV ratio and the Pauli coherence: it reaches a maximum at BBCH 20 to 30, depending on the parcel, and after a short plateau it starts to decrease monotonically until the end of the season. This trend confirms the main objective of such a decomposition: the volume scattering increases progressively with respect to the polarized component (which is due to both the double-bounce and the differential extinction) as the plants develop from the vegetative phase to the end. More extra information is provided by α_P. This angle behaves similarly to α_1 until BBCH 45-50; however, from BBCH 45 it remains around 45 degrees (corresponding precisely to the double-bounce filtered by the extinction at the vegetation volume) because with this approach the random volume contribution is better separated (since a model-based decomposition is being used) and the observed polarized component still behaves like expected. Only at the very end (BBCH 80) α_P diverges from 45 degrees. Note that α_1 was lower than 45 degrees from BBCH 50 for all parcels, since the eigenvector decomposition does not provides this physically based separation between a random volume and a polarized scattering mechanism. In conclusion, and despite the cross-polar channel is not available in the data, this decomposition is useful to confirm the presence of volume scattering at the end of the season.

Finally, by extracting the main features commented in this section, next section presents a strategy to retrieve the phenological stage of rice fields based on their polarimetric signature.

V. Retrieval of phenology

According to the previous analysis, and despite the BBCH scale providing precise phenological information in the dynamic range between 0 and 100, it is enough for most practical purposes to define a set of intervals of phenological development with similar physical characteristics. These physical features are translated into the radar response of the scene as expected ranges for some polarimetric observables. In this work the following five phenological intervals have been defined:

1. Early vegetative phase (BBCH 0–17)
2. Transition at plants emergence (BBCH 18–21)
3. Advanced vegetative phase (BBCH 22–49)
4. Reproductive phase (BBCH 50–69)
5. Maturation (BBCH 70+)

The definition of the actual algorithm for estimating the phenological stage can be regarded as the solution of a classification problem, where each class corresponds to a phenological interval, and can be identified in the observation space defined by a set of parameters.

From the explanations in the previous section, we can conclude that none of the observables can be used alone to define a phenology retrieval algorithm, since there is not a direct relationship between phenology and any single observable for the full range of phenology stages. Instead, some observables exhibit different ranges of values at some stages or intervals, thus helping to identify particular phenological intervals from the rest. Just as examples, the coherence between HH and VV is only high at the beginning of the growth cycle, or α_1 is stable around 45 degrees during the advanced vegetative phase. Therefore, the strategy for defining the retrieval algorithm consists in choosing a set of polarimetric parameters and their corresponding ranges for each stage, in such a way that their joint observation results in a classification as less ambiguous as possible. In this sense, several parameters may offer similar behaviors, so most of the phenological intervals can be identified in an equivalent way by several parameters.

In this work the interest is placed in showing the potential for this application of physically based observables, so we have not employed any automatic approach (e.g. support vector machines) for defining the best set of input parameters or the optimum thresholds, and that task is left for future research. In addition, it is important to mention that the analysis performed so far has been based on a single average value for each parcel and image, and therefore the intrinsic variability of each parameter has not been taken into account. This variability or statistical uncertainty is caused both by the potential scene heterogeneity and by the estimation procedure itself. For instance, the standard deviation of the measured phases (like $\Delta\phi$ and δ) depends on the number of looks employed in the averaging and also on the associated coherences ($|\rho_{hhvv}|$ and $|\rho_P|$, respectively).

For simplicity, in the proposed approach four parameters have been selected for establishing the retrieval algorithm, namely: entropy (H), dominant scattering mechanism (α_1), and magnitude and phase of the correlation between HH and VV ($|\rho_{hhvv}|$ and $\Delta\phi$). Note again that other parameters would be also valid, but a full comparison in terms of performance and accuracy is out of the scope of this manuscript. The rationale for assigning a phenological stage (one out of the five defined intervals) to a pixel is as follows: a pixel is assigned to a stage when all the parameters used to define this stage are within a predefined range. The decision space is graphically sketched in Figure 5 by using the 2D planes formed by H and α_1, and $|\rho_{hhvv}|$ and $\Delta\phi$, respectively. Note that not all the parameters are used for defining every stage. The predefined ranges are justified in the following:

1. Early vegetative phase: $\alpha_1 < 30^\circ$ and $|\rho_{hhvv}| > 0.6$

Two different informations that describe the surface-type scattering which characterizes this stage are combined. From Figure 2b, there are only high values of copolar coherence at the beginning of the season, but this coherence is not much lower in other stages, like in the advanced vegetative one. Hence, the additional use of α_1, which in turn characterizes a surface-type mechanism when it is close to zero, makes this decision more robust. On the other hand, α_1 should not be used alone as a criterion for assigning this stage because it also presents low values at the maturation stage. It is only by combining both that a reli-

able estimate is obtained.
In addition, those pixels presenting a very low backscatter in both copolar channels (less than -16 dB) are directly assigned to this stage, since they can be assumed to correspond to the water surface when the wind induced roughness is not strong enough.
2. Plant emergence: $\alpha_1 > 30°$ and $0.3 < |\rho_{hhvv}| < 0.6$ and $H > 0.65$ and $\Delta\phi < -90°$
This narrow interval has been found to exhibit in most cases a clearly distinct behavior with respect to the previous and the following stages. In fact, its identification is only possible if the image is acquired at the moment the plants are emerging and there is a mixed response from the rough water at the ground and the double bounce between stems/tillers and the ground. In such cases entropy increases and the phase difference between HH and VV is very pronounced, so these two parameters are used to define this stage. In addition, the possible ranges of $|\rho_{hhvv}|$ and α_1 have been differentiated with respect to the previous stage to reduce the probabilities of misclassifying between both types.
3. Advanced vegetative phase: $40° < \alpha_1 < 55°$ and $H < 0.65$
This stage is well defined by only two parameters: entropy, which is low, and dominant scattering mechanism, which characterizes a dipole-like response because the scattering is very polarized as discussed previously in the text.
4. Reproductive phase: $30° < \alpha_1 < 40°$ and $|\rho_{hhvv}| < 0.3$ and $0.65 < H < 0.9$
Both this stage and the maturation one present low coherences between HH and VV. Regarding H and α_1, they progressively drift to extreme values (higher for entropy and lower for α_1), starting in this stage and continuing in the maturation. Therefore, an arbitrary threshold has been established for both parameters in order to separate this stage from the following one.
5. Maturation: $\alpha_1 < 30°$ and $|\rho_{hhvv}| < 0.3$ and $H > 0.9$
As just commented, this stage presents low values of $|\rho_{hhvv}|$, as the reproductive one, but a higher entropy and a lower α_1.

Before testing this algorithm, it is important to note that the proposed retrieval algorithm does not cover the whole observation space, in the sense that there are pixels which will fall outside the specified ranges and, therefore, will be left not assigned to any phenological stage. This option has been preferred because in a very final application, when the phenological stage has to be decided for a field or parcel on a majority basis, those unclassified pixels would not interfere into a correct estimation. In other words, it is more convenient to leave unclassified pixels rather than misclassified ones.

For illustration purposes, retrieval results will be shown by applying the algorithm at pixel level, i.e. providing a phenological stage for each multi-looked pixel and not for each parcel, since it provides additional information about the features that can be found within a parcel at some dates. Since the estimation of all polarimetric observables treated in this work requires an averaging or multi-looking, a boxcar window of 15x15 pixels (ENL = 68) has been applied. The resulting spatial resolution is 13 m x 38 m approximately. Uncertainties provided by this estimation for each observable can be found in [16]. Note that the spatial resolution of the SLC images required for this application can be derived by knowing the size of the minimum element to be identified within a field (e.g. a spot with advanced or delayed development with respect to its parcel due to local conditions) and the minimum ENL providing accurate estimates of the involved polarimetric observables. Approximately, if spots of 10-20 m have to be detected, the required spatial resolution of the input images will be around 1-3 m.

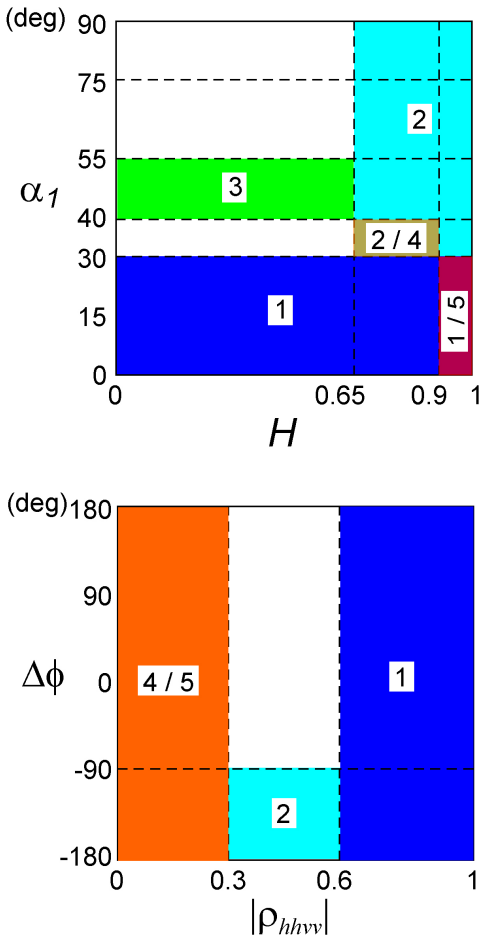

Fig. 5. Scheme of the decision space on the two planes defined by H and α_1 (left), and $|\rho_{hhvv}|$ and $\Delta\phi$ (right). Codes: 1: Early vegetative. 2: Plants emergence. 3: Advanced vegetative. 4: Reproductive. 5: Maturation

Figure 6 shows the results of applying this algorithm at all dates on the area occupied by parcel F. The general evolution of the phenology of the parcel is tracked very well. As a validation test, the stage assigned to the majority of pixels at every date agrees with the BBCH measured in the ground campaign at the same date. By inspecting these images, additional aspects can be commented as follows.

During the first three dates, the field is quite homogeneous and the early vegetative phase is well estimated for almost the whole parcel area. Only at the third date (DoY 159) a few small wrong spots (assigned to later stages) appear in the lowest subparcel. Then, at DoY 170 the parcel reaches the stage defined as transition at plants emergence. However, there are large areas in two sub-parcels which still belong to the previous stage, since they are less developed, and also some sparse pixels are wrongly classified as belonging to the last stage. Moving to the next date (DoY 181), most of the left parts of the sub-parcels have evolved to the advanced vegetative phase, but the right parts (including those assigned before to the early vegetative phase)

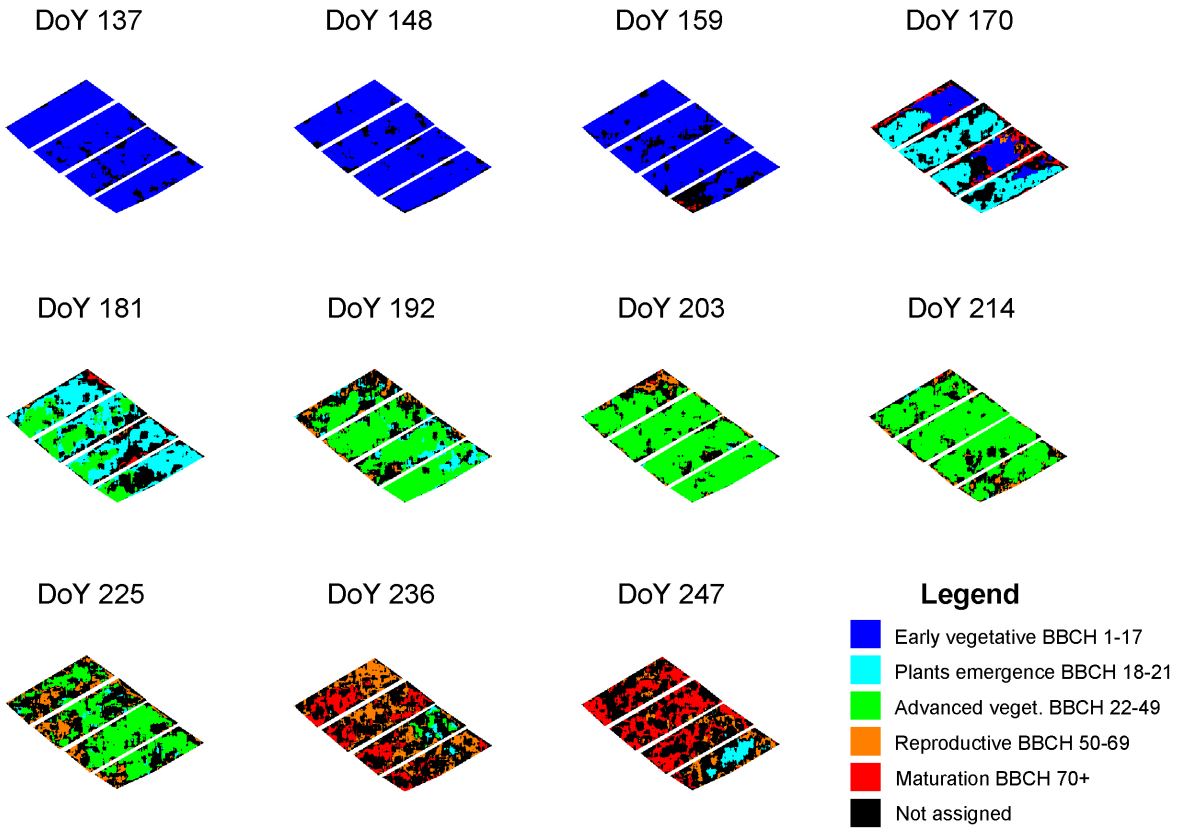

Fig. 6. Estimated phenology at the location of parcel F for all acquisitions at 30 degrees incidence, as provided by the single acquisition algorithm. A boxcar window of 15x15 pixels (68 looks) has been applied to the input images for speckle filtering and averaging.

are well identified as pertaining to the plants emergence stage. Therefore, one can appreciate in these results that the left parts of the sub-parcels are developing slightly faster than the right parts. The few red points appearing in the image at DoY 181 are a residual result of the ambiguity already mentioned in the text between this stage and the maturation one.

Images acquired at DoY 192, 203 and 214 correspond to the advanced vegetative phase, with a vast majority of pixels correctly assigned to this stage. Anyway, there exist a small percentage of pixels classified as belonging to the reproductive stage. These errors come mainly from the arbitrary thresholds used in this simple algorithm (see Figure 5), instead of searching for optimized ones, but the performance of the algorithm is quite satisfactory despite its relative simplicity.

Date 225 establishes the beginning of the transition to the reproductive stage, since the number of pixels assigned to this stage is larger than before. Again, the left part of the sub-parcels reach the more advanced development stages sooner. Then, at DoY 236 the left part of the sub-parcels already shows important spots at the maturation stage, whereas the right part of one sub-parcel is still in the vegetative phase. Most of the pixels, however, pertain to the reproductive phase as expected from the ground measurements. This heterogeneity in the phenological evolution has been confirmed by the farmers.

Finally, most of pixels reach the maturation phase at the last image (DoY 247), despite there is still a significant percentage of them assigned to the previous reproductive phase. In this last image there appear also a number of pixels assigned to the plants emergence phase and even to the early vegetative stage. This is a consequence of the high entropy that characterizes this scenario at that moment, thus reducing the reliability of the polarimetric information provided by the images. However, the actual phenological stage is well estimated on a parcel basis, which is a noteworthy result.

Although the images in Fig. 6 correspond to only one parcel, similar results have been obtained for the rest of monitored fields, thus confirming the validity of the proposed approach. Some problems have been found only in two specific dates over parcel B and a portion of parcel C. They correspond to scenarios where the transition at plants emergence is not well discriminated from the last two stages (reproductive and maturation) because the double-bounce scattering coming from the new plants does not dominate yet above the surface scattering from the flooded ground. Then, entropy is high and the dominant scattering mechanism is still well below 45 degrees (see plots in Figure 2). In such particular cases, both stages cannot be distinguished with dual-pol data only, and quad-pol measurements would be required. However, the availability of dual-pol HHVV data measured in a coherent way yields the important advantage, over incoherent dual-pol measurements, of solving in most cases the ambiguity between the transition at plants emergence and the last two stages. Both situations are characterized by similar absolute backscattering levels and ratios (HH/VV), so they cannot be distinguished in any way with incoherent measurements in a single acquisition approach, unless extra information is available. Hence, coherent measurements of both channels

outperform incoherent acquisitions for this purpose.

In conclusion, in most cases the right phenological phase (in a range of five meaningful intervals) has been retrieved by employing just a single TerraSAR-X image (in coherent HHVV dual-pol mode), and hence the main objective of this work has been achieved.

VI. Conclusions and future work

The exploitation of coherent HHVV dual-pol X-band imagery, provided by the TerraSAR-X satellite, for monitoring the phenological cycle of rice fields has been analyzed in this work. A series of 15 images have been processed and a set of polarimetric observables has been computed from them. The radar response of the rice fields has been interpreted by means of these observables in terms of the scattering mechanisms and polarization effects present in the scene at different phenological stages. Then, a simple procedure to estimate the phenological stage (from a set of five possible intervals) from a single acquisition has been proposed and tested.

Despite the simplicity of the proposed approach, the capability of this remote sensing technique to retrieve the phenological stage of rice fields at a particular date has been demonstrated, based on the availability of an HHVV dual-pol image measured coherently. This coherence in the acquisition of the copolar channels is essential to enable the retrieval approach to work with just a single acquisition, since the ambiguities present in the backscatter levels (and their ratio) can be avoided by combining other observables in a proper way. This solution has produced correct phenology estimates in most cases. In a few locations, however, the dual-pol configuration is not enough, and we have found high entropies that may correspond to either the presence of two dominant scattering mechanisms, like in the moment of plants emergence, or to a strongly depolarizing scene, as at the end of the growth cycle. A potential discrimination between these two situations would be based, if available, on fully polarimetric measurements, since they are characterized by very different anisotropy values, for instance.

The main limitations of this approach originate from the system specifications, namely: a narrow swath (around 15 km on the ground) which is too small for devising a monitoring scheme on large scale rice plantations, and a high noise level (NESZ around -19 dB) similar to the backscattering level from rice fields, especially at the early stages of the cultivation cycle. The use of a fully polarimetric imaging mode would provide a solution to the second issue, besides its potential for avoiding ambiguities in the data interpretation and for a more complete scene modeling and target decomposition, since noise can be estimated and removed consistently from the data as explained in [19]. To increase the coverage for monitoring large sites, multiple acquisitions with different beams and ascending/descending passes could be combined.

Future work about this topic will include a full statistical analysis for deciding the best set of observables, and their corresponding ranges, for a phenology retrieval algorithm based on just one acquisition, including other possible classification or decision strategies. Statistical uncertainties and other estimation issues will be taken into account. Moreover, a wider ground campaign, with more parcels and more detailed information about crops information and local heterogeneities at parcel level should be performed. If possible, new experiments over other regions with different rice varieties and cultivation practices could be carried out in order to extend these ideas to other scenarios of evident interest (e.g. SE Asia). Finally, the effect of weather conditions (especially rain and wind) and the presence of other crop types within the rice fields should be considered and treated in the design of a practical tool for the farmers.

From the final application point of view, the incorporation of additional information will be studied. For instance, techniques based on time series, also including multiple acquisitions with different incidence angles and ascending/descending passes, could help to both improve the results at a single date (in terms of robustness and increased precision in the BBCH scale) and provide a shorter refresh rate of the results, which may be necessary for some precision farming practices. Moreover, auxiliary information available at the end-user level (i.e. farmers) could be incorporated in the devise of algorithms to deliver final products related with this remote sensing area.

Acknowledgments

The authors would like to thank the support of Manuel Cano, Fernando Carrascal and Santiago Aparicio, all from the Federacion de Arroceros de Sevilla, for providing the ground measurement data and for their helpful comments.

All SAR images have been provided by DLR in the framework of projects LAN0021 and LAN0234 of the pre-launch AO of TerraSAR-X.

Thanks to Dr. Iain H. Woodhouse and his group for supporting this project by hosting a sabbatical of Juan M. Lopez-Sanchez at the Edinburgh Earth Observatory, January-September 2010.

Appendix

Dual-pol model-based target decomposition

In the fully polarimetric case a 3x3 coherency matrix is decomposed into the sum of three coherency matrices corresponding to oriented volume scattering, surface scattering and double-bounce scattering. By assuming a reflection symmetric scene, as rice fields are, the measured coherency matrix reduces to:

$$[T_3] = \begin{bmatrix} t_{11} & t_{12} & 0 \\ t_{12}^* & t_{22} & 0 \\ 0 & 0 & t_{33} \end{bmatrix} \tag{1}$$

and the mentioned decomposition can be expressed as [10]:

$$[T_3] = m_V[T_{V3}] + m_S[T_{S3}] + m_{DB}[T_{DB3}] \tag{2}$$

where the individual matrices of surface and double bounce take the following forms:

$$[T_{S3}] = \begin{bmatrix} \cos^2\alpha_s & \cos\alpha_s \sin\alpha_s e^{j\phi_s} & 0 \\ \cos\alpha_s \sin\alpha_s e^{-j\phi_s} & \sin^2\alpha_s & 0 \\ 0 & 0 & 0 \end{bmatrix} \tag{3}$$

$$[T_{DB3}] = \begin{bmatrix} \cos^2\alpha_d & \cos\alpha_d \sin\alpha_d e^{j\phi_d} & 0 \\ \cos\alpha_d \sin\alpha_d e^{-j\phi_d} & \sin^2\alpha_d & 0 \\ 0 & 0 & 0 \end{bmatrix} \tag{4}$$

The contribution from the volume is usually described by two parameters: X which characterizes the particles shape and dielectric properties, and Δ which corresponds to the width of the angular distribution assuming it is uniform [10][2]. It is common to further assume that the particles behave as dipoles, so X is large and the coherency matrix of the volume term results in:

$$[T_{V3}] = \begin{bmatrix} 2 & 2\frac{\sin 2\Delta}{2\Delta} & 0 \\ 2\frac{\sin 2\Delta}{2\Delta} & 1+\frac{\sin 4\Delta}{4\Delta} & 0 \\ 0 & 0 & 1-\frac{\sin 4\Delta}{4\Delta} \end{bmatrix} \quad (5)$$

Finally, when the distribution of particles in the volume is fully random ($\Delta = \pi/2$), the volume component reduces to the following form, which corresponds to a scene with full azimuthal symmetry:

$$[T_{V3}] = \begin{bmatrix} 2 & 0 & 0 \\ 0 & 1 & 0 \\ 0 & 0 & 1 \end{bmatrix} \quad (6)$$

The mentioned simplifications are employed in most cases to reduce the dimensionality of the inverse problem, since the number of independent observations (values in the observed coherency matrix) must be larger or equal than the unknowns or parameters to be retrieved.

In the fully polarimetric case, if we assume that a scene is characterized by a random volume component as in (6) plus the two polarized contributions defined in (3–4), a common way to solve the decomposition starts by retrieving the volume component m_V directly from the t_{33} element, which is provided by the cross-polar signal. Then, the remaining terms are estimated by assuming that one of the two mechanism dominates and assigning the corresponding parameters accordingly [10].

An important issue of this approach is that after extracting the volume component, the remaining data must correspond to a physical scene, which mathematically means that the remaining coherency matrix has to be positive semidefinite. Otherwise, the remaining power contributions to be estimated (m_S and m_{DB}) could result negative, hence non-physical. Therefore, in order to avoid such a problem, the estimation of m_V is carried out ensuring that the remaining matrix after the volume extraction is still positive semidefinite (a matrix with rank 2, or with non-negative eigenvalues). In this way, the total coherency matrix is decomposed as a random volume component plus a rank-2 matrix (i.e. RV+rank2) [10], [16].

It is evident from the previous discussion that we would need fully polarimetric data to retrieve the parameters of the three components present in rice scenes. Since we have available only dual-pol data (with coherency matrices defined by four parameters: two real numbers and a complex one), we will employ the following two hypotheses in order to formulate this decomposition. Firstly, despite we have described the vegetation volume of rice fields as an oriented volume (OV), the direct scattering from the stems and tillers (i.e. from the vertically oriented particles) is expected to be low because the main scattering is directed from these cylinder-like particles to the specular direction (which in turn generates the double-bounce due to the presence of the flooded ground). Therefore, if some direct backscattering is expected from the particles they should be oriented in a fashion different from vertical and, in the limit, randomly oriented. Consequently, the scattering component due to the volume can be approximated by the RV model defined in (6). The second assumption deals with the other two contributions: surface and double-bounce mechanisms. Since only dual-pol data are at disposal, in the definition of the decomposition we have to assume they will not be present simultaneously. From the analysis presented in Section IV, this will be true from the end of the plants emergence stages onwards (i.e. from BBCH 22 approximately).

Under these hypotheses, the measured dual-pol coherency matrix can be decomposed to find a random volume (RV) component plus a rank-1 remaining matrix. Being a rank-1 matrix, it corresponds to a polarized component, so a subscript P will be used for denoting the parameters of this component. It is important to note that the type of scattering of the remaining rank-1 mechanism will be defined by its corresponding α_P angle parameter, so it is not necessary to know a priori its origin.

In summary, the analytical expression of the proposed RV plus rank-1 decomposition is the following:

$$[T_2] = m_V[T_{V2}] + m_P[T_{P2}] \quad (7)$$

where

$$[T_{V2}] = \begin{bmatrix} 2 & 0 \\ 0 & 1 \end{bmatrix} \quad (8)$$

$$[T_{P2}] = \begin{bmatrix} \cos^2\alpha_P & \cos\alpha_P \sin\alpha_P e^{j\phi_P} \\ \cos\alpha_P \sin\alpha_P e^{-j\phi} & \sin^2\alpha_P \end{bmatrix} \quad (9)$$

so we will obtain four parameters (m_V, m_P, α_P, ϕ_P) from the four real numbers that define the coherency matrix $[T_2]$.

A specific aspect of the proposed RV+rank1 decomposition is the estimation of the volume component without using the cross-polar channel, which is usually employed for that purpose in this type of approach. We have also tested this point with Radarsat-2 data by comparing the parameters retrieved with the RV+rank2 from the full 3x3 coherency matrix against the estimates provided by the RV+rank1 from the 2x2 upper-left coherency submatrix. The differences in the retrieved amount of volume scattering ($2m_V$) were always below 2.5 dB, so it provides an acceptable estimate for this type of analysis.

Finally, the final analytical expression of the parameters retrieved by this decomposition, which guarantees that all decomposition products are positive semi-definite (i.e. physically valid components), is presented in the following:

$$m_V = \frac{1}{4}\left(T_2(1,1) + 2T_2(2,2) - \sqrt{(T_2(1,1)+2T_2(2,2))^2 - 8|T_2|}\right) \quad (10)$$

$$m_P = T_2(1,1) + T_2(2,2) - 3m_V \quad (11)$$

$$[T_{sd}] = [T_2] - m_V \begin{bmatrix} 2 & 0 \\ 0 & 1 \end{bmatrix} \quad (12)$$

[2]Similar expressions can be derived when other distributions are employed for the angular orientation.

$$e_2 = \frac{m_P - T_{sd}(1,1)}{T_{sd}(1,2)} \tag{13}$$

$$\alpha_P = \arccos\left(\frac{1}{\sqrt{1+|e_2|^2}}\right) \tag{14}$$

$$\phi_P = \arg(e_2) \tag{15}$$

where $[T_{sd}]$ is the matrix remaining after the subtraction of the volume component, and e_2 is a complex number employed for presenting an explicit expression of the parameters of the polarized component.

REFERENCES

[1] T. Kurosu, M. Fujita, and K. Chiba, "Monitoring of rice crop growth from space using the ERS-1 C-band SAR," *IEEE Trans. Geosci. Remote Sensing*, vol. 33, no. 4, pp. 1092–1096, July 1995.

[2] T. Le Toan, F. Ribbes, L.-F. Wang, N. Floury, K.-H. Ding, J. A. Kong, M. Fujita, and T. Kurosu, "Rice crop mapping and monitoring using ERS-1 data based on experiment and modeling results," *IEEE Trans. Geosci. Remote Sensing*, vol. 35, no. 1, pp. 41–56, Jan. 1997.

[3] J.-Y. Koay et al., "Paddy fields as electrically dense media: Theoretical modeling and measurement comparisons," *IEEE Trans. Geosci. Remote Sensing*, vol. 45, no. 9, pp. 2837–2849, Sept. 2007.

[4] A. Bouvet, T. Le Toan, and N. Lam-Dao, "Monitoring of the rice cropping system in the Mekong delta using ENVISAT/ASAR dual polarization data," *IEEE Trans. Geosci. Remote Sensing*, vol. 47, no. 2, pp. 517–526, Feb. 2009.

[5] T. Le Toan, H. Laur, E. Mougin, and A. Lopes, "Multitemporal and dual-polarization observations of agricultural vegetation covers by X-band SAR images," *IEEE Trans. Geosci. Remote Sensing*, vol. 27, no. 6, pp. 709–718, Nov. 1989.

[6] Y. Inoue et al., "Season-long daily measurements of multifrequency (Ka, Ku, X, C, and L) and full-polarization backscatter signatures over paddy rice field and their relationship with biological variables," *Remote Sensing of Environment*, vol. 81, pp. 194–204, 2002.

[7] J. M. Lopez-Sanchez, J. D. Ballester-Berman, and I. Hajnsek, "First results of rice monitoring practices in Spain by means of time series of TerraSAR-X dual-pol images," *IEEE J. Selected Topics in Applied Earth Observations and Remote Sensing*, vol. 4, no. 2, pp. 412–422, June 2011.

[8] F. T. Ulaby, D. N. Held, M. C. Dobson, K. C. McDonald, and T. B. A. Senior, "Relating polarization phase difference of SAR signals to scene properties," *IEEE Trans. Geosci. Remote Sensing*, vol. 25, no. 1, pp. 83–92, Jan. 1987.

[9] J.-S. Lee, M. R. Grunes, and E. Pottier, "Quantitative comparison of classification capability: Fully polarimetric versus dual and single-polarization SAR," *IEEE Trans. Geosci. Remote Sensing*, vol. 39, no. 11, pp. 2343–2351, Nov. 2001.

[10] S. R. Cloude, *Polarisation. Applications in remote sensing*, Oxford University Press, 2009.

[11] J. C. Zadoks, T. T. Chang, and C. F. Konzak, "A decimal code for the growth stages of cereals," *Weed Research*, vol. 14, no. 6, pp. 415–421, Dec. 1974.

[12] U. Meier, Ed., *Growth Stages of Mono- and Dicotyledonous Plants. BBCH Monograph*, 2nd edition, 2001, http://www.jki.bund.de/fileadmin/dam_uploads/_veroeff/bbch/BBCH-Skala_englisch.pdf.

[13] T. Fritz et al., *TerraSAR-X Ground Segment. Level 1b Product Format Specification. Annex B*, DLR. Doc. TX-GS-DD-3307, 2007, http://sss.terrasar-x.dlr.de/pdfs/TX-GS-DD-3307.pdf.

[14] T. Fritz, "Tips & tricks for spectral, radiometric and geometric interpretation of TerraSAR-X products. Part I," in *Proceedings of the 3rd TerraSAR-X Science Team Meeting*, Wessling, Germany, Nov. 2008, http://sss.terrasar-x.dlr.de/papers_sci_meet_3/tricks/TSX-products_tips_and_tricks-1.pdf.

[15] T. Fritz et al., *TerraSAR-X Ground Segment. L1b Product Phase Pattern Correction*, DLR. Doc. TX-GS-TN-3031, 2010.

[16] J.-S. Lee and E. Pottier, *Polarimetric radar imaging. From basics to applications*, CRC Press, 2009.

[17] S. R. Cloude, "The dual polarization entropy/alpha decomposition: a PALSAR case study," in *Proceedings of the 3rd PolInSAR Workshop*, Frascati, Italy, Jan. 2007.

[18] A. Freeman and S. L. Durden, "A three-component scattering model for polarimetric SAR data," *IEEE Trans. Geosci. Remote Sensing*, vol. 36, no. 3, pp. 963–973, May 1998.

[19] I. Hajnsek, K. P. Papathanassiou, and S. R. Cloude, "Removal of additive noise in polarimetric eigenvalue processing," in *Proceedings of IEEE IGARSS*, Sydney, Australia, July 2001, vol. 6, pp. 2778–2780.

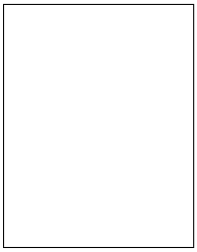

Juan M. Lopez-Sanchez (S'94, M'00, SM'05) was born in Alicante, Spain, in 1972. He received the Ingeniero and Doctor Ingeniero degrees in Telecommunication Engineering from the Technical University of Valencia (UPV), Valencia, Spain, in 1996 and 2000, respectively. From 1998 to 1999 he worked as a predoctoral grantholder at the Space Applications Institute, Joint Research Centre of the European Commission, Ispra, Italy. Since 2000 he leads the Signals, Systems and Telecommunication Group of the University of Alicante, Spain, where he is full professor since November 2011.

His main research interests include microwave remote sensing for inversion of biophysical parameters, polarimetric and interferometric techniques, SAR imaging algorithms and analytical and numerical models for multiple scattering problems.

In 2001, Dr. Lopez-Sanchez received the INDRA award for the best Ph.D. thesis about radar in Spain. Since 2006 he is the Chair of the Spanish Chapter of the IEEE Geoscience and Remote Sensing Society. He has coauthored more than 30 papers in refereed journals and more than 60 papers and presentations in international conferences and symposia.

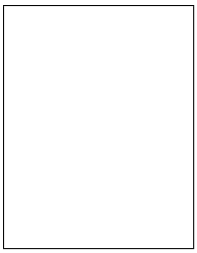

Shane R. Cloude (M'87, SM'96, F'01) received the B.Sc. degree from the University of Dundee, Dundee, U.K., in 1981, and the Ph.D. degree from the University of Birmingham, Birmingham, U.K., in 1987. He was a Radar Scientist at the Royal Signals and Radar Establishment (RSRE), Great Malvern, U.K., until 1987. Following this, he held teaching and research posts at the University of Dundee, the University of York, U.K., and the University of Nantes, France, before taking on his present role in 1996. He is currently Director and Senior Scientist with Applied Electromagnetic Consultants (AELc), Edinburgh, U.K., undertaking contract research on a range of problems associated with radar and optical remote sensing.

Dr Cloude is a Fellow of the IEEE, the Alexander von Humboldt Society in Germany and honorary Fellow of the School of Geosciences, University of Edinburgh.

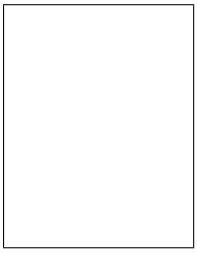

J. David Ballester-Berman was born in Xixona, Spain. He received the Ingeniero degree in telecommunications engineering from the Technical University of Valencia, Spain, in 2000, and the Doctor Ingeniero degree in telecommunications engineering from the University of Alicante, Spain, in 2007. From 2000 to 2001, he was a Support Engineer in the development of software tools for the planning and design of terrestrial digital television systems. Since 2001, he has been with the Signals, Systems, and Telecommunication Group of the University of Alicante, carrying out educational and research tasks.

His research interests include microwave remote sensing for biophysical parameter retrieval, polarimetric SAR interferometry techniques, and electromagnetic modeling of vegetation covers.